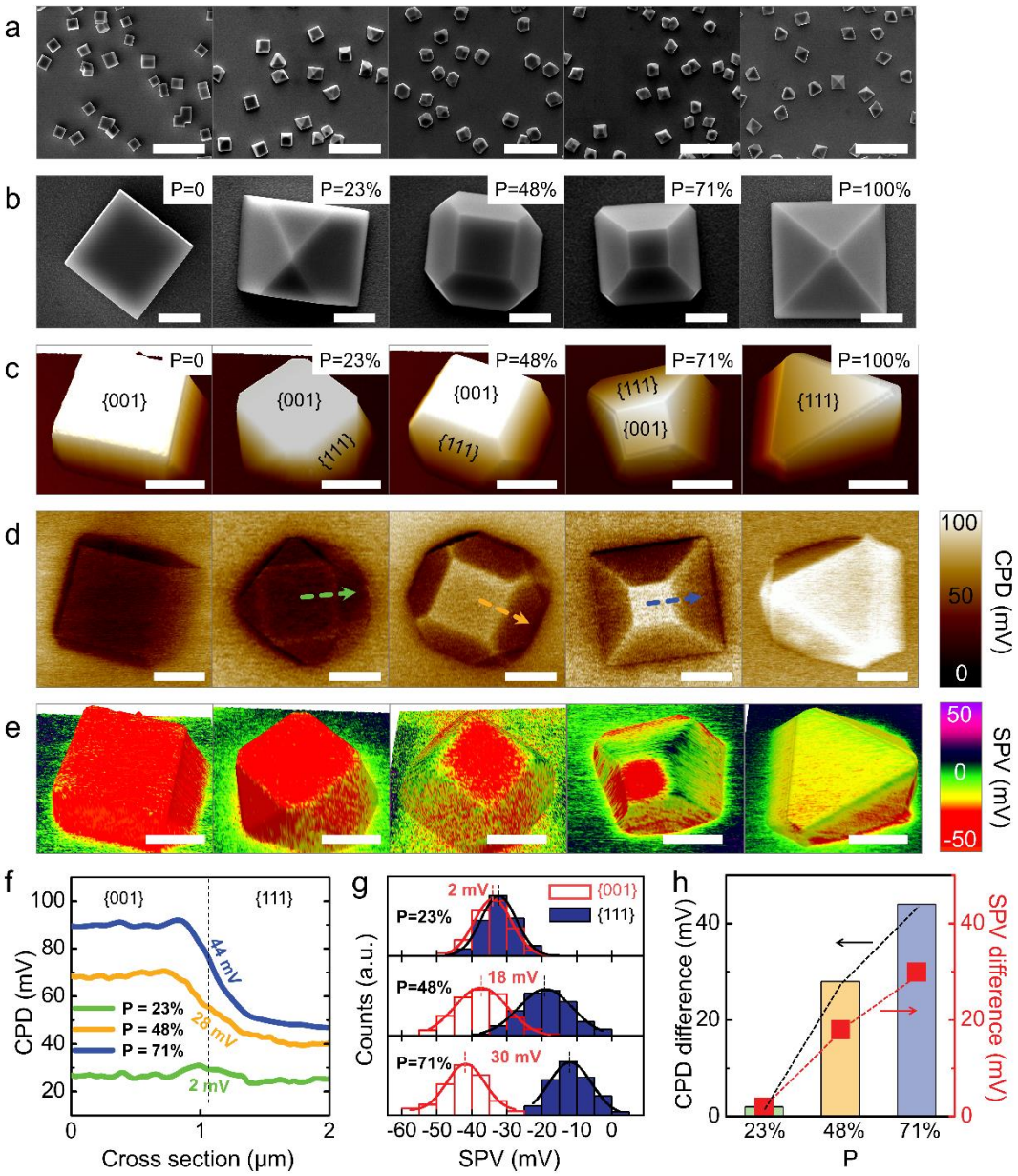

Extended Data Fig. 1 | Anisotropic facet engineering of Cu_2O particles. a–e, SEM images at low magnification (**a**) and high magnification (**b**). AFM images (**c**), KPFM images (**d**), and SPVM images (**e**) of Cu_2O particles with morphologies varying from cube to octahedron. Scale bars: (**a**) 20 μm and (**b–e**) 2 μm. Proportions (P) are defined as P = S{111} / (S{001} + S{111}), where S{111} and S{001} represent areas of the {111} and {001} facets, respectively. Proportions are 0%, 23%, 48%, 71%, and 1% for Cu_2O particles from the leftmost panel to the rightmost panel. KPFM images show that

the surface potential (CPD) signals increase with P, indicating a gradually decreasing p-type doping level from facet {001} to {111}, suggesting anisotropic V_{Cu} distributions. The higher surface potential of the {001} facet than that of the {111} facet on a truncated octahedral particle suggests higher p-type doping near the {001} facet, since the two facets share the same Fermi energy. SPVM images show negative signals, indicating electron transfer to the surface and that more electrons are distributed on the {001} facet. **f**, Surface potential distributions across the {001} and {111} facets indicated as lines in **d**. **g**, Histograms of SPV signals extracted from the {001} and {111} facets of polyhedral Cu_2O particles with various morphologies. Gaussian fits are used to determine the averaged signals. **h**, Correlation between CPD and SPV signals based on differences between the {001} and {111} facets of polyhedral Cu_2O particles with various morphologies. Data extracted from **f** and **g**.

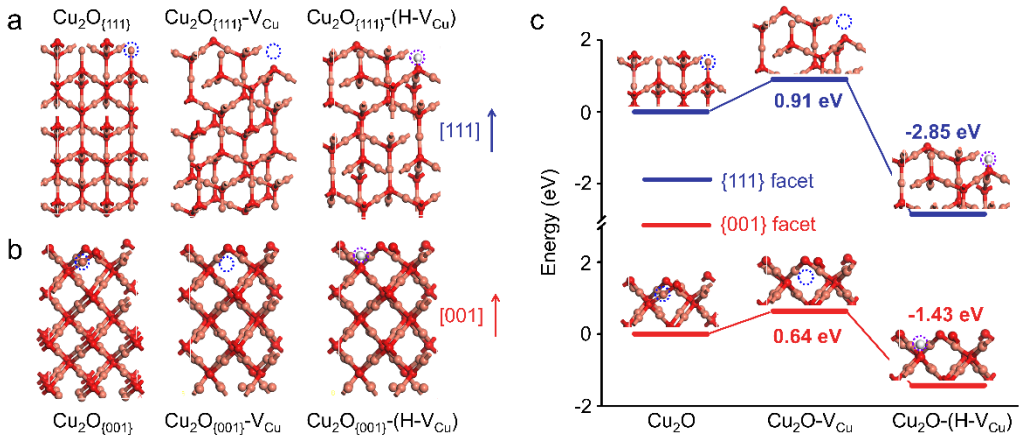

Extended Data Fig. 2 | DFT calculations a,**b**, Optimized structures of {001} (**a**) and {111} (**b**) surfaces of Cu_2O with and without V_{Cu} or (H–V_{Cu}) defects, as denoted. Red, pink, and white spheres represent O, Cu, and H, respectively. **c**, Calculated formation energies of V_{Cu} and (H–V_{Cu}) defects on the {001} and {111} facets. Results indicate that V_{Cu} and (H–V_{Cu}) defects are likely to be formed on the {001} and {111} facets, respectively.

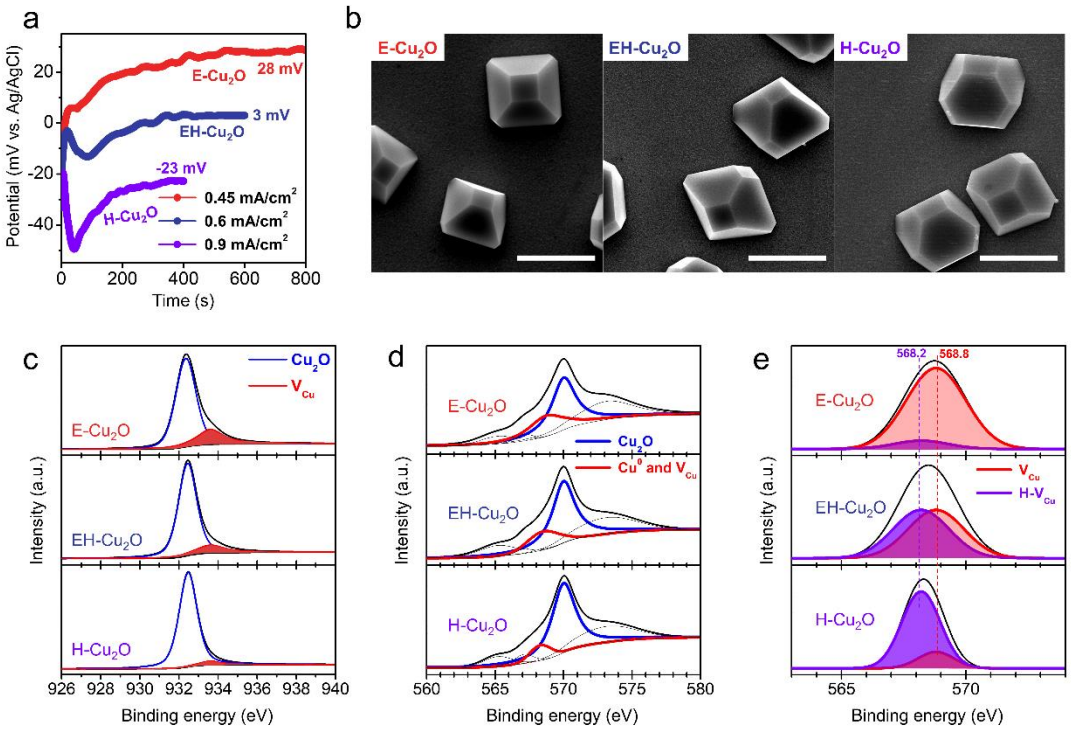

Extended Data Fig. 3 | Defect engineering of truncated octahedral Cu_2O particles. **a**, Potential–time curves of galvanostatic growth of E–Cu_2O, EH–Cu_2O, and H–Cu_2O particles. **b**, SEM images of E–Cu_2O, EH–Cu_2O, and H–Cu_2O particles. Scale bars, 5 μm. **c** XPS spectra of defect-engineered Cu_2O particles. Binding energies of Cu 2p3/2 peaks in Cu_2O estimated to be 932.6, 932.4, and 933.6 eV for Cu^0, Cu^+, and Cu^{2+}, respectively.[42] Measured Cu 2p3/2 peaks fitted as a composition of two contributions with maxima of approximately 932.4 and 933.6 eV, corresponding to Cu_2O and V_{Cu}, respectively. Contribution of V_{Cu} decreases from E–Cu_2O to H–Cu_2O. **d** Fits of Cu LMM Auger peaks. Two main peaks at 570.0 eV (Cu_2O, blue line) in the range 568.2–568.8 eV (an overlap of Cu^0 and Cu^{2+}, red line) and three peaks at 573.1, 567.1, and 565.2 eV indicate that different transitions states of Cu LMM spectrum are considered in the fits.[29] **e**, Deconvoluted Auger Cu LMM spectra in Cu^0 and Cu^{2+} overlap range. Characteristic binding energies of Cu^0 and Cu^{2+} are 568.2 and 568.8 eV, respectively,

corresponding to (H-V_{Cu}) and V_{Cu} defects, respectively. Proportions of Cu^0 and Cu^{2+} increase and decrease from E–Cu_2O to H–Cu_2O, respectively, indicating increased (H–V_{Cu}) defects and decreased V_{Cu} defects from E–Cu_2O to H–Cu_2O.

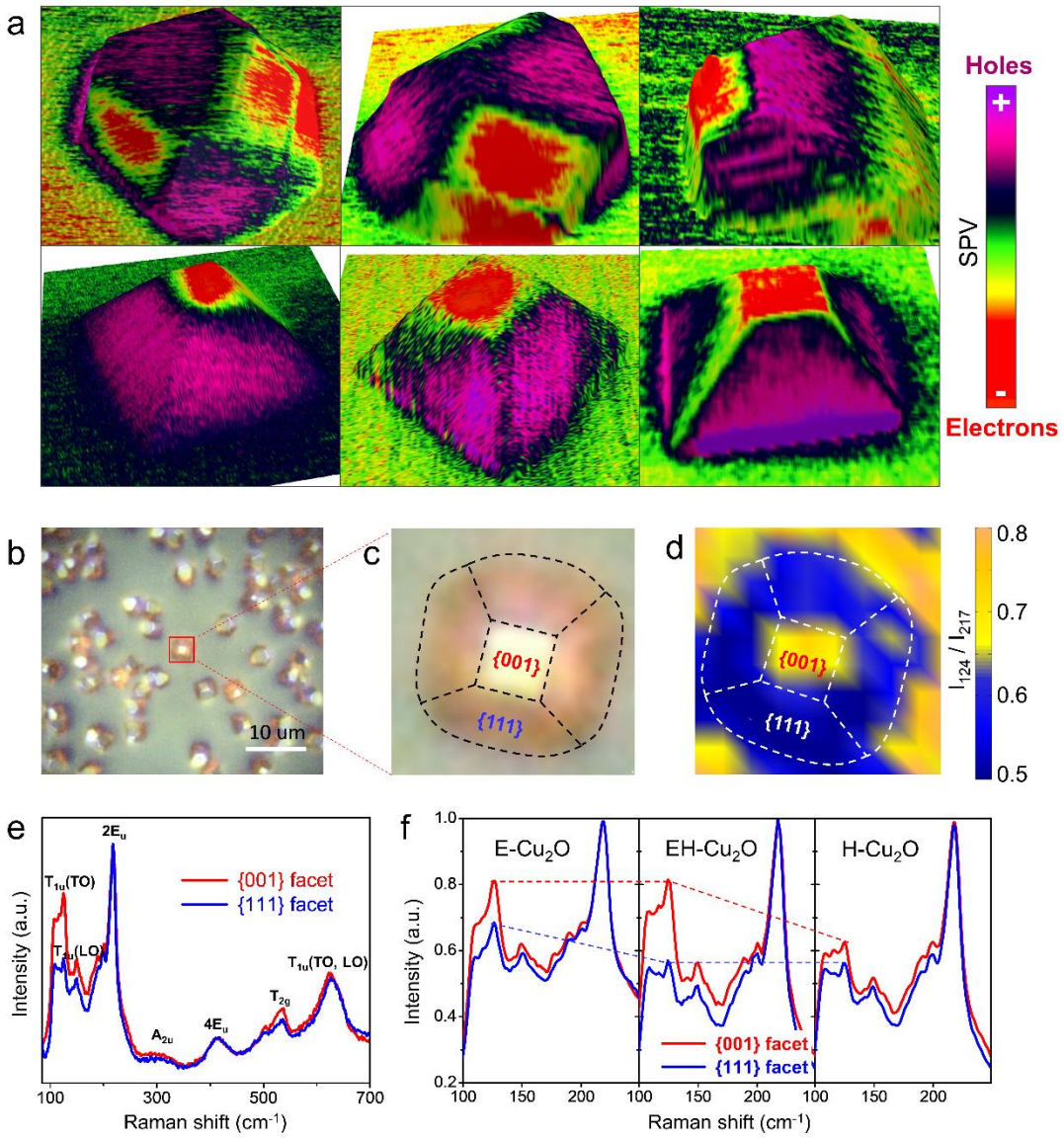

Extended Data Fig. 4 | Reproducibility of spatially separated electron and hole distributions and spatially resolved defect distributions of EH–Cu_2O particles. a, SPVM images of EH–Cu_2O particles from six batches, where the samples were synthesized at different times. SPV results of E–Cu_2O and H–Cu_2O were reproducible but are not shown herein owing to limited space. **b**, Optical image of EH–Cu_2O particles. **c**, Zoomed-in view from red box in **b**. **d**, Raman microscopy image of particle in **c** mapped by peak intensity ratio of T_{1u} (TO) and $2E_u$ phonon modes. **e**, Raman spectra collected on the {001} and {111} facets of EH-Cu_2O particles. Spectra show

typical Raman peaks of cubic phase Cu_2O, assigned as shown in the figure based on previous reports[20]. T_{1u} (TO) phonon mode is related to copper vacancy defects[20]. $2E_u$ phonon mode is intrinsic to Cu_2O crystals owing to strong coupling to yellow excitation and hence can be used as a reference[43]. **f**, Quantitative comparison of T_{1u} (TO) Raman peak intensity with reference to $2E_u$ Raman peak intensities of E–Cu_2O, EH–Cu_2O, and H–Cu_2O samples.

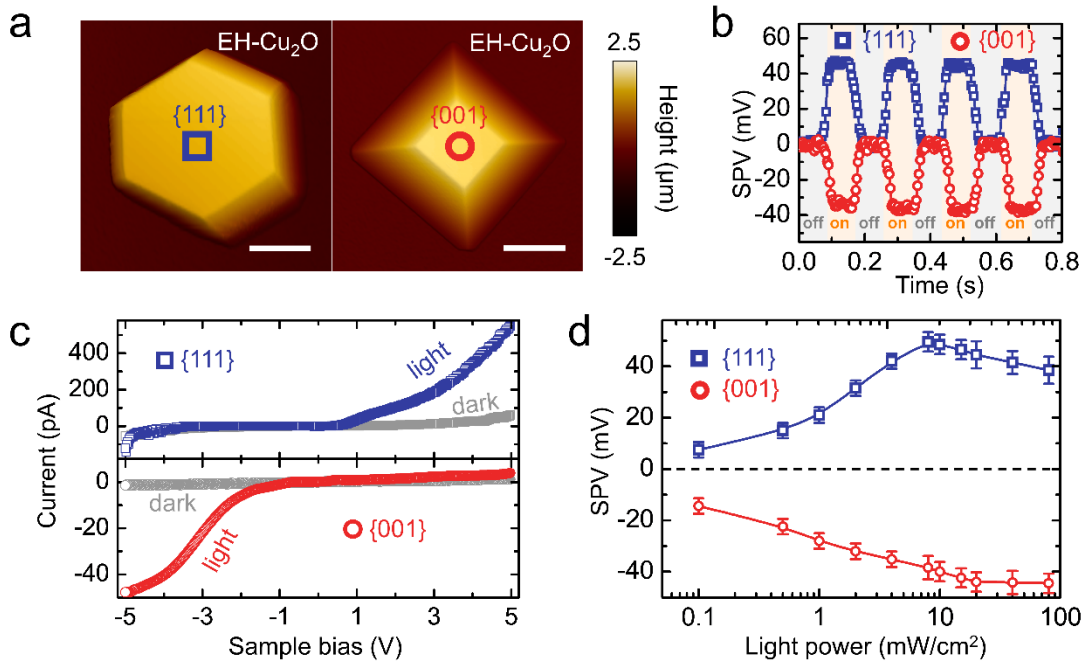

Extended Data Fig. 5 | Modulated measurements of localized charge transfer in EH–Cu_2O particles. **a**, AFM images of EH–Cu_2O particles used for modulation measurements. Scale bars, 2 μm. **b**, SPV signals collected on {111} and {001} facets of EH–Cu_2O particles in **a** and measured under 6 Hz chopped light illumination. **c**, I–V curves collected from the {111} and {001} facets of EH–Cu_2O particles in **a** and measured under dark (gray line) and 450-nm illumination (blue and red lines) via conductive atomic force microscopy. **d**, Dependence of SPV signals on light power measured from the {111} and {001 facets of EH–Cu_2O particles in **a**. Error bars are based on electronic noise in modulated SPV measurements via external lock-in amplifier.

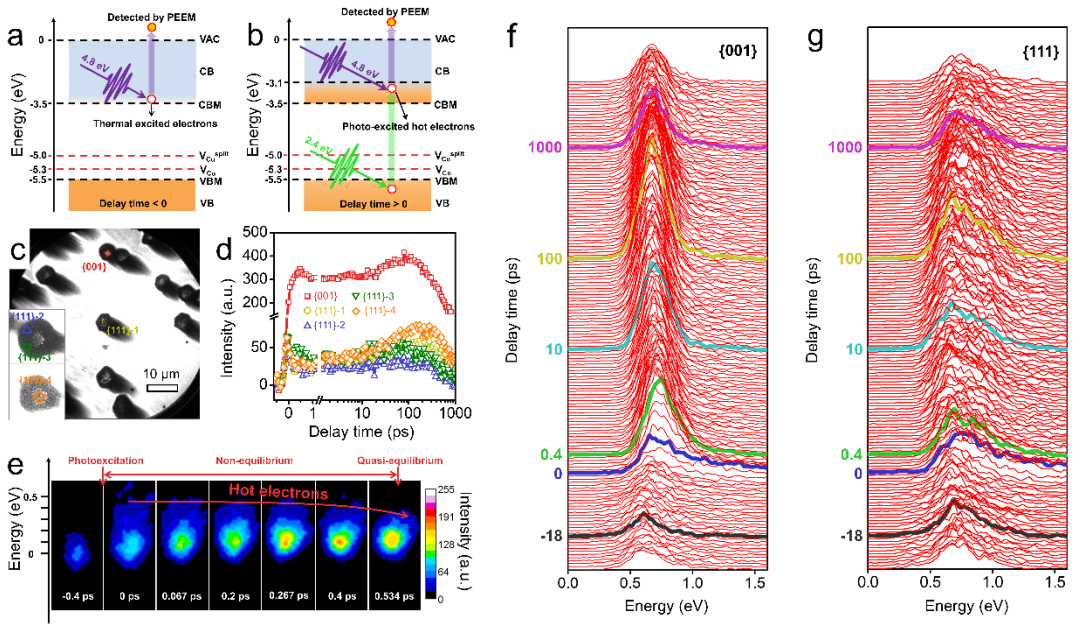

Extended Data Fig. 6 | Time-resolved photoemission electron microscopy of EH–Cu_2O particles. a,**b**, Schematic illustration of energy path of electrons with negative (**a**) and positive (**b**) pump–probe delay times. VAC, CB, CBM, VC_u^{split}, V_{Cu}, VBM, and VB defined as vacuum energy level (VAC), conduction band (CB), conduction band minimum (CBM), energy level of split copper vacancy (V_{Cu}^{split}), energy level of a simple copper vacancy (V_{Cu}), valence band maximum (VBM), and valence band (VB), respectively. Vacuum energy level is set to 0 eV. Energy level of CBM is determined from ref. 44. Bandgap is determined to be approximately 2.0 eV from UV-vis absorption spectrum. Energy levels of V_{Cu} and V_{Cu}^{split} located at 0.2–0.3 eV and 0.4–0.5 eV above VBM[45]. No donor levels exist near CBM in Cu_2O[45]. **c**,**d**, Reproducibility of facet-dependent photoelectron dynamics (**d**) on other EH–Cu_2O particles, as shown in PEEM images (**c**). Photoelectron dynamics of top and side {111} facets, as labeled, are almost consistent, indicating minimal effect of electric field distortion in PEEM imaging on our system. **e**, Energy distributions of electrons obtained from the {001}

facet of the EH–Cu_2O particle detected in energy-resolved mode at different pump–probe delay times, as labeled. Energy benchmark (0 eV) is set at a position where the photoelectron intensity is maximum before photoexcitation. Significant increase in photoelectron intensity within 0.5 ps provides evidence of ultrafast separation of photogenerated electrons toward {001} surface. High-energy electrons observed within 0.5 ps indicate existence of non-equilibrium hot electrons. Maximum broadening of photoelectron distribution toward higher energies is 0.4–0.5 eV, consistent with energy distribution of hot electrons before thermalization for a Cu_2O band gap of 1.9–2.0 eV and pump energy of 2.4 eV. **f**,**g**, Energy distribution spectra of photo-emitted electrons obtained at the {001} facet (**f**) and {111} facet (**g**) of EH–Cu_2O particles at different delay times. Delay times span -47 ps to approximately 1700 ps from bottom to top. Characteristic time delays are labeled. Peak positions of photoelectron spectra at delay times from -47 to -1 ps are averaged; subsequently, the averaged peak position is set as the benchmark.

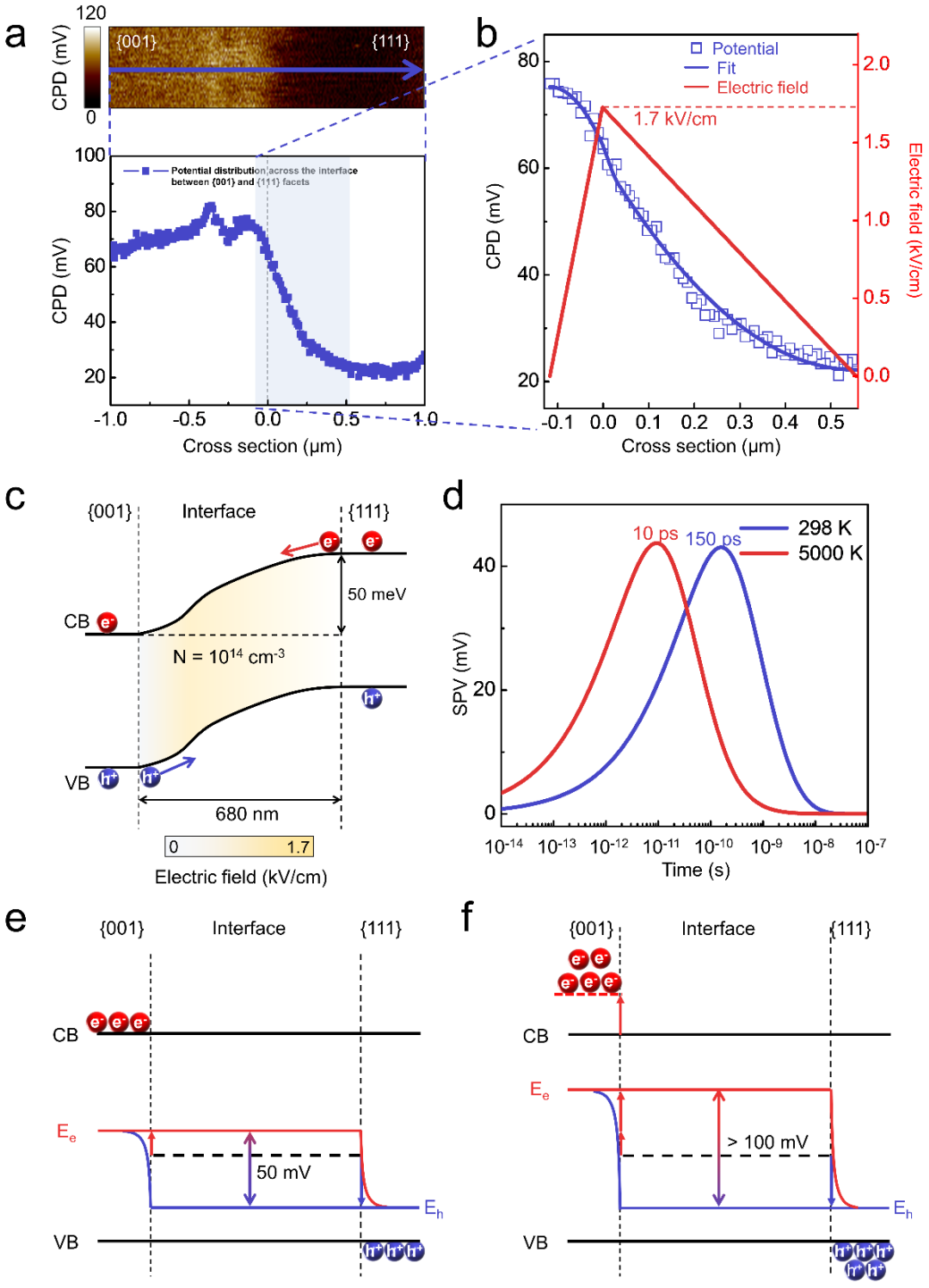

Extended Data Fig. 7 | Charge transfer mechanism between {001} and {111} facets of EH–Cu_2O particles. a, Potential distribution across interface between {001} and {111} facets. KPFM image mapped with tip lift height of 10 nm to minimize crosstalk effects. **b**, Fitting of potential distribution and strength of interfacet built-in electric

field. Fitting is conducted using an abrupt junction model; doping density on the order of ~10^{14} cm^{-3} and electric field strength 1.7 kV/cm were provided. **c**, Established band diagram at the interface between the {001} and {111} facets. **d**, Evolution of SPV signals with time calculated using conventional drift–diffusion model (see Methods for details). Calculation was based on model established in **c**. **e**, **f.** Illustration shows SPV generation induced by charge transfer in drift–diffusion model (**e**) or in ballistic regime (**f**).

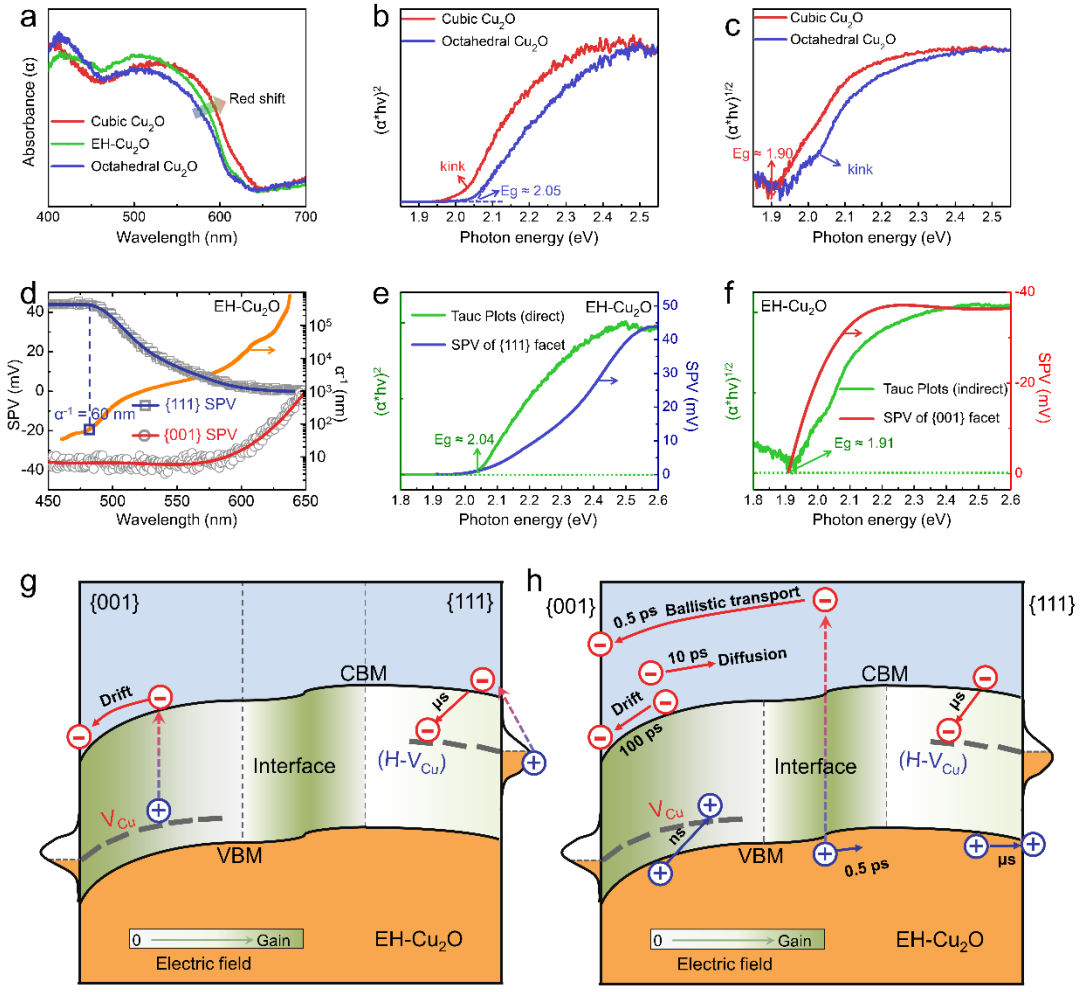

Extended Data Fig. 8 | Facet-dependent absorption and schematic illustration of charge transfer in EH–Cu_2O particles. a, Diffuse reflectance spectra of cubic Cu_2O, EH–Cu_2O and octahedral Cu_2O. **b**,**c**, Tauc plots for cubic and octahedral Cu_2O particles in direct transition regime (**b**) and indirect transition regime (**c**). Tauc plots show that absorption of {001} facets (cubic Cu_2O) reflects indirect transition with bandgap (E_g) of ~1.91 eV, and that absorption of {111} facets (octahedral Cu_2O) reflects direct transition with E_g of ~2.05 eV. **d**, Spatially resolved SPV spectra of the {001} and {111} facets of EH–Cu_2O and spectral-dependent absorption length of Cu_2O (data after Malerba et al[46]). As positive SPV signals are related to (H–V_{Cu})-induced trapping, the

signals can reflect distribution of (H–V_{Cu}) defects in depth. SPV signals on the {111} facet reach a maximum at an excitation wavelength below ~480 nm, corresponding to an absorption length of ~60 nm. Results indicate that the (H–V_{Cu}) defects are primarily distributed within 60 nm at near-surface regions on the {111} facet. **e**, Tauc plots of direct transitions for EH–Cu_2O and SPV spectrum obtained from the {111} facet of EH–Cu_2O. Onset of Tauc plots of direct transitions agree well with SPV spectrum of the {111} facet; hence, absorption edge of the {111} facet of EH–Cu_2O is determined to be ~2.04 eV. **f**, Tauc plots of indirect transitions for EH–Cu_2O and SPV spectrum obtained from the {001} facet of EH–Cu_2O. Onset of Tauc plots of indirect transitions agree well with SPV spectrum of the {001} facet; hence, absorption edge of the {001} facet of EH–Cu_2O is determined to be ~1.91 eV. **g**, Schematic illustration of charge separation on the {001} and {111} facets of EH–Cu_2O with sub-bandgap excitation. **h**, Schematic illustration of complete charge transfer processes in EH–Cu_2O.

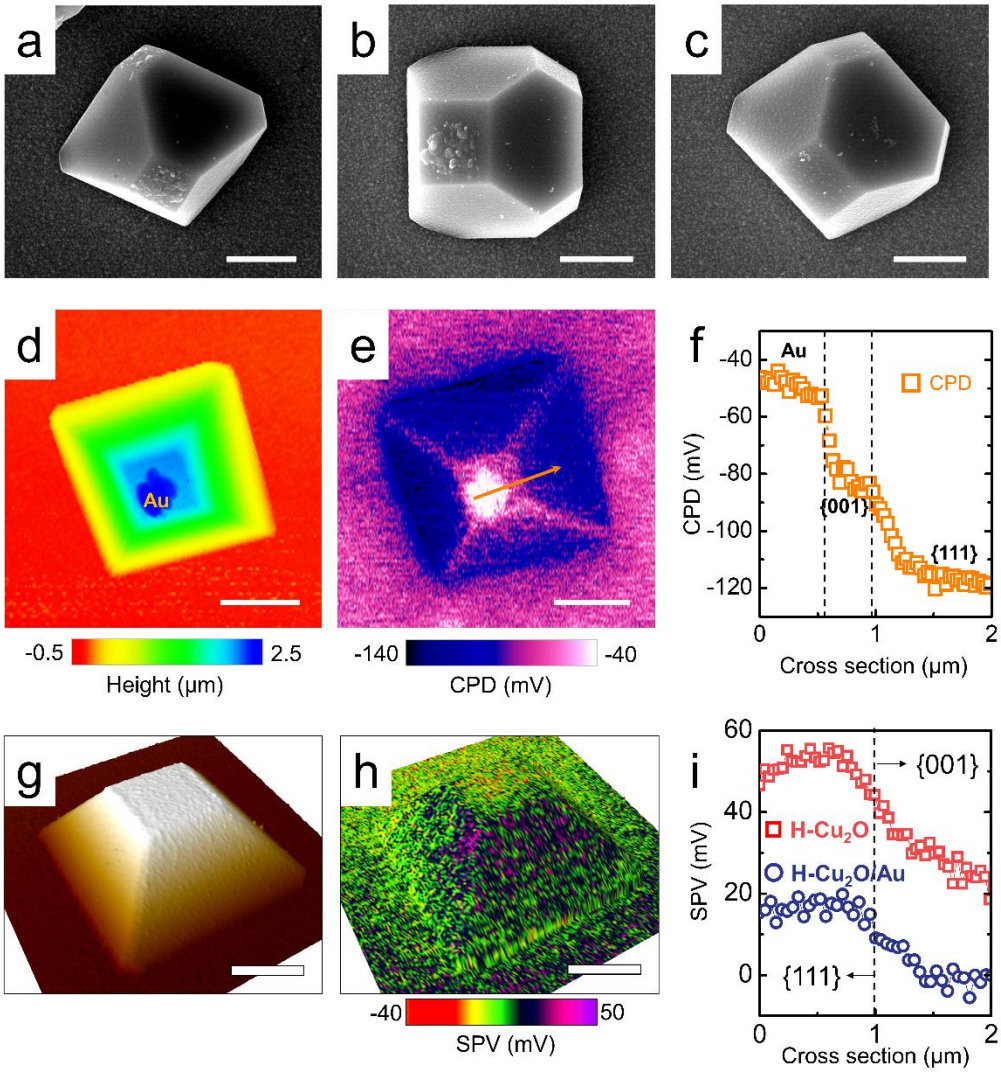

Extended Data Fig. 9 | Photodeposition of Au on Cu_2O particles. a–c, SEM images of EH–Cu_2O (**a**), E–Cu_2O (**b**), and H–Cu_2O (**c**) with photodeposition of Au. Samples denoted as EH–Cu_2O/Au, E–Cu_2O/Au, and H–Cu_2O/Au, respectively. Scale bars, 2 μm. **d**,**e**, AFM image (**d**), and corresponding KPFM image (**e**) of EH–Cu_2O/Au particle. **f** CPD distributions along line **e**. Quantitative data showing local increase in surface potential at Au sites, demonstrating enhanced built-in electric field. **g**,**h**, AFM image (**g**), and corresponding SPVM image (**h**) of EH–Cu_2O/Au particle. **i**, Comparison of SPV distributions across the {111} and {001} facets before and after Au deposition on H–Cu_2O particles.

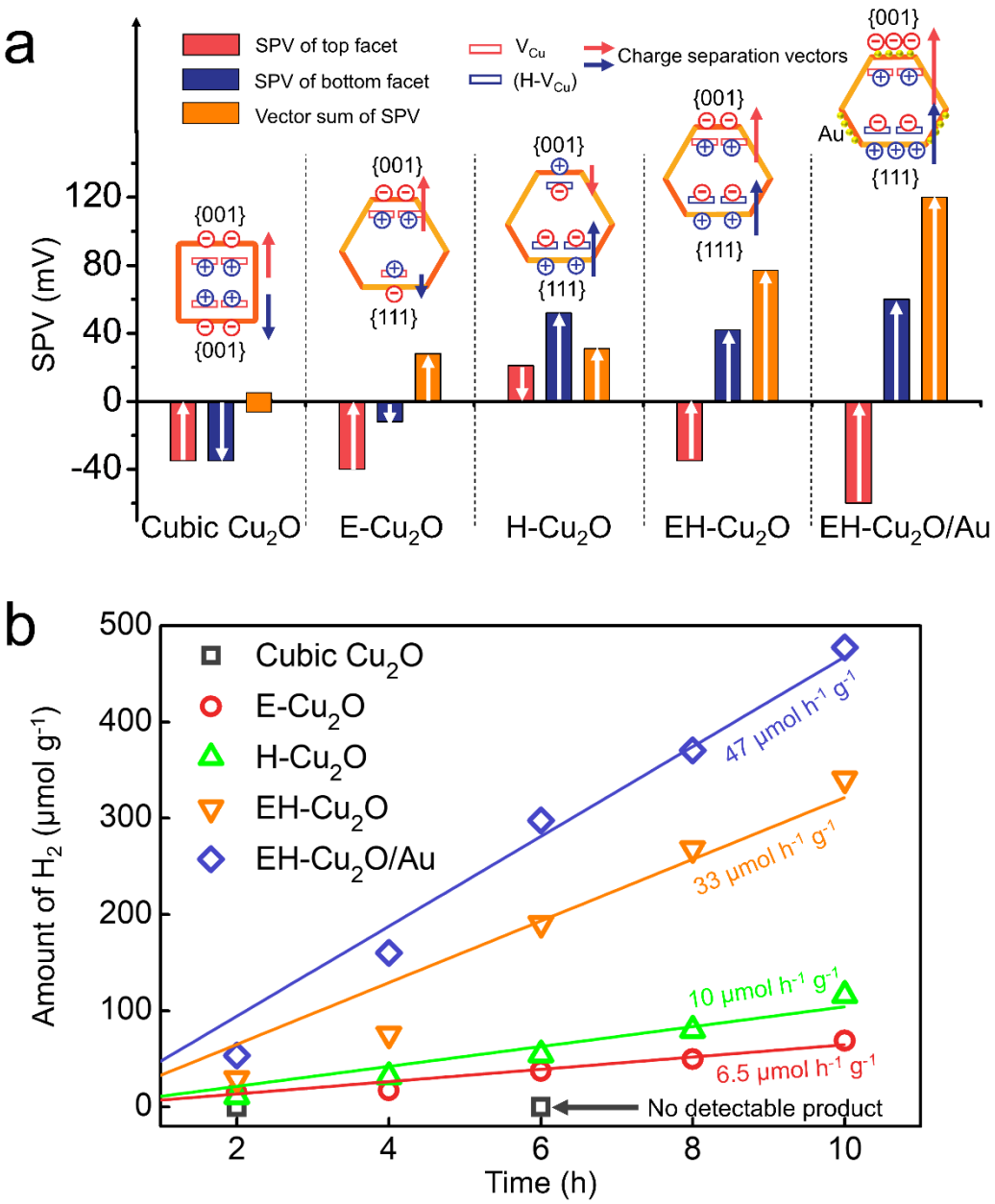

Extended Data Fig. 10 | Driving force of anisotropic charge transfer and photocatalytic performance of Cu_2O particles. a, Determination of driving force of anisotropic charge transfer in Cu_2O photocatalytic particles with vector sum of spatially resolved SPV signals. **b**, Time course of photocatalytic H_2 evolution for different Cu_2O photocatalyst particles. Lines represent linear fits for determining rate of H_2 generation.